Using high-order polynomial basis in 3-D EM forward modeling based on volume integral equation method

Originally published in:
Geophysical Journal International 213(2), https://doi.org/10.1093/gji/ggy059

Geophysical Journal International

Geophys. J. Int. (2018) **213,** 1387–1401
Advance Access publication 2018 February 14
GJI Geomagnetism, rock magnetism and palaeomagnetism

doi: 10.1093/gji/ggy059

Using high-order polynomial basis in 3-D EM forward modeling based on volume integral equation method

Mikhail Kruglyakov and Alexey Kuvshinov

Institute of Geophysics, ETH Zurich, CH-8092 Zurich, Switzerland. E-mail: m.kruglyakov@gmail.com

Accepted 2018 February 13. Received 2018 January 29; in original form 2017 May 29

SUMMARY

3-D interpretation of electromagnetic (EM) data of different origin and scale becomes a common practice worldwide. However, 3-D EM numerical simulations (modeling)—a key part of any 3-D EM data analysis—with realistic levels of complexity, accuracy and spatial detail still remains challenging from the computational point of view. We present a novel, efficient 3-D numerical solver based on a volume integral equation (IE) method. The efficiency is achieved by using a high-order polynomial (HOP) basis instead of the zero-order (piecewise constant) basis that is invoked in all routinely used IE-based solvers. We demonstrate that usage of the HOP basis allows us to decrease substantially the number of unknowns (preserving the same accuracy), with corresponding speed increase and memory saving.

Key words: Electromagnetic theory; Geomagnetic induction; Magnetotellurics; Numerical modelling.

1 INTRODUCTION

In geophysics, electromagnetic (EM) methods aim to resolve generally 3-D distributions of subsurface electrical conductivity. Since conductivity depends on rock type and composition, temperature and fluid/melt content, these methods are widely used in academia and industry. To interpret EM data, the EM field which is governed by Maxwell's equations needs to be computed for a given model of 3-D conductivity distribution. Here, we restrict our task by considering only the frequency-domain formulation. Usually, a large number of such simulations are required and complex, detailed and large-scale 3-D models are invoked. Thus, EM (forward) solvers that are able to deliver fast and accurate computation of the EM field are essential.

The EM forward solvers can be distinguished by the numerical techniques utilized. Three basic techniques are used in geoelectromagnetism, namely finite-difference (FD), finite-element (FE) and volume integral equation (IE) methods. For decades FD-based solvers (Mackie *et al.* 1994; Haber & Ascher 2001; Newman & Alumbaugh 2002; Egbert & Kelbert 2012, among others) dominated in EM due to the rather straightforward implementation of the FD concept. However, in recent years, FE-based (Schwarzbach *et al.* 2011; Farquharson & Miensopust 2011; Puzyrev *et al.* 2013; Ren *et al.* 2013; Um *et al.* 2013; Grayver & Burg 2014, among others) and IE-based (Avdeev *et al.* 2002; Hursan & Zhdanov 2002; Singer 2008; Koyama *et al.* 2008; Kamm & Pedersen 2014; Kruglyakov *et al.* 2016, among others) solvers have increased in popularity due to methodological developments of the latter two methods.

One of the main differences between the FE and IE methods lies in the structure and size of the resulting system matrices. In the IE method, one works with compact (but dense) matrices. The reason for compactness is that boundary conditions are exactly accounted for Green's functions, and thus the modeling region is confined only to 3-D conductivity structures (anomalies) under investigations. By contrast, in the FE method, one has to discretize a much larger volume laterally and vertically in order to enable the decay (or stabilization) of the EM field at the boundaries of the modeling domain. However, this advantage is counterbalanced by the fact that FE matrices are sparse. Another distinction between the methods is that the condition number (which controls the stability of the solution) of system matrices in FE depends on discretization and frequency, whereas in IE—it does not, provided a particular class of IE with a contracting kernel is exploited (Singer 1995; Pankratov *et al.* 1995; Zhdanov 2002). On the other hand, the FE method more easily treats the models with topography or/and bathymetry. It is pertinent to note here that all previous EM IE solvers (except the solver discussed in Farquharson & Oldenburg 2002), used the zero-order polynomial (piecewise constant; PWC) basis to describe the EM field behaviour within a modeling domain. Despite this, until recently, they demonstrated comparable efficiency with FE solvers based on a trilinear basis, in terms of accuracy and required computational resources.

Recently, Grayver & Kolev (2015) showed that the usage of the second-order polynomial basis in FE solvers allows a decrease in the number of unknowns by several orders of magnitude and thus greatly speeds up EM field simulations. Inspired by this result, we developed an IE solver which exploits a high-order polynomial (HOP) basis, and demonstrate that it indeed outperforms the IE solver based on a PWC basis.

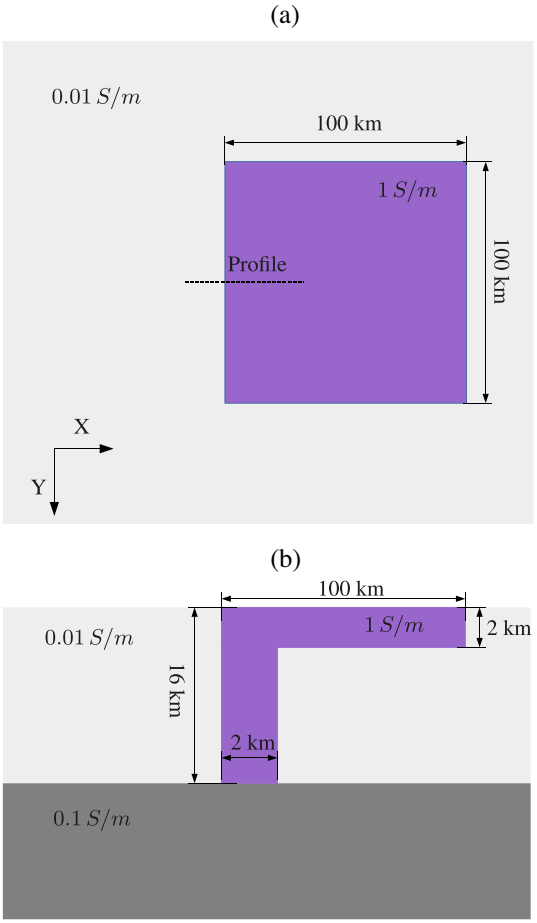

Figure 1. Fault model. Top (a)—a plan view of the model and bottom (b)—side view. The dashed line in the upper plot depicts the profile along which MT apparent resistivities are shown in Fig. 2.

2 INTEGRAL EQUATION APPROACH

Let the complex-valued function $\sigma(M)$, $\mathbf{Re}\,\sigma(M) \geq 0$ be a 3-D conductivity distribution in space. We search for the electric, $\mathbf{E}$, and magnetic, $\mathbf{H}$, fields induced by an electric current, $\mathbf{J}_{\text{ext}}$, in the model with conductivity $\sigma(M)$. These fields obey the system of Maxwell's equations

$$\begin{cases} \text{curl}\,\mathbf{H} = \sigma\mathbf{E} + \mathbf{J}_{\text{ext}}, \\ \text{curl}\,\mathbf{E} = i\omega\mu_0\mathbf{H}. \end{cases} \tag{1}$$

Here, $i = \sqrt{-1}$, ω is an angular frequency, and μ_0 is the magnetic permeability of free space. Time dependence of all fields is accounted for by $e^{-i\omega t}$. Let $\Omega \subset \mathbb{R}^3$ be some bounded domain, $\sigma(M) = \sigma_b(z)$ for $M(x, y, z) \notin \Omega$, and $\sigma(M) = \sigma_a(M)$ for $M \in \Omega$. Then, for any $M \in \mathbb{R}^3$, the fields $\mathbf{E}(M)$ and $\mathbf{H}(M)$ are expressed in terms of the integrals

$$\mathbf{E}(M) = \mathbf{E}^b(M) + \int_\Omega \widehat{G}_E(M, M_0)\Delta_\sigma(M_0)\mathbf{E}(M_0)d\Omega_{M_0}, \tag{2}$$

$$\mathbf{H}(M) = \mathbf{H}^b(M) + \int_\Omega \widehat{G}_H(M, M_0)\Delta_\sigma(M_0)\mathbf{E}(M_0)d\Omega_{M_0}. \tag{3}$$

Here, $\Delta_\sigma = \sigma_a - \sigma_b$ and $\widehat{G}_E$, $\widehat{G}_H$ are electric and magnetic Green's tensors, respectively (*cf.* Pankratov *et al.* 1995). The fields $\mathbf{E}^b$ and $\mathbf{H}^b$ in eqs (2) and (3) are called the background (normal) electric and magnetic fields and they obey the following system of Maxwell's equations

$$\begin{cases} \text{curl}\,\mathbf{H}^b = \sigma_b(z)\mathbf{E}^b + \mathbf{J}_{\text{ext}}, \\ \text{curl}\,\mathbf{E}^b = i\omega\mu_0\mathbf{H}^b. \end{cases} \tag{4}$$

Note, that the dependence on frequency of all the above quantities is omitted but implied. Note also, that $\widehat{G}_E$ and $\widehat{G}_H$ are dependent on the background conductivity σ_b.

Table 1. Details of successful runs with HOP and PWC IE solvers for the model depicted in Fig. 1. $\tilde{N}_z$ stands for the number of unknowns in vertical direction. In PWC case $\tilde{N}_z = N_z$, in HOP case $\tilde{N}_z = 4N_z$, where 4 arises since the third-order polynomial basis is used. Time is that required for two polarizations modeling.

Run with	$\tilde{N}_z$	Number of unknowns	RAM (GB)	Time (CPU × hours)
PWC	128	96×10^6	427	17
HOP	8	6×10^6	17	2

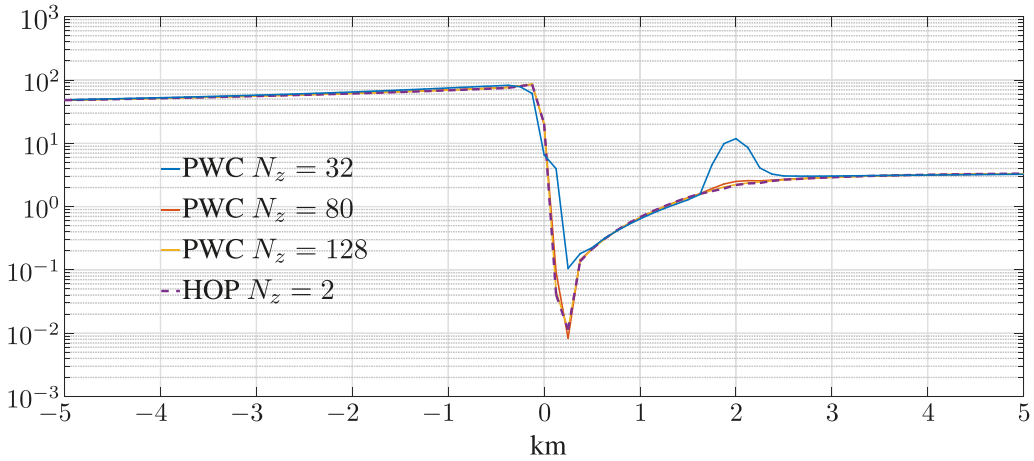

Figure 2. Apparent resistivity ρ_{xy} (at period 1000 s) along the profile shown in Fig. 1(a). Solid (blue, red and yellow) curves are the results obtained with the use of the PWC IE solver. The colours distinguish between the results of modelings with different numbers of cells in the vertical direction, N_z. The dashed curve stands for the results obtained with the use of the HOP IE solver.

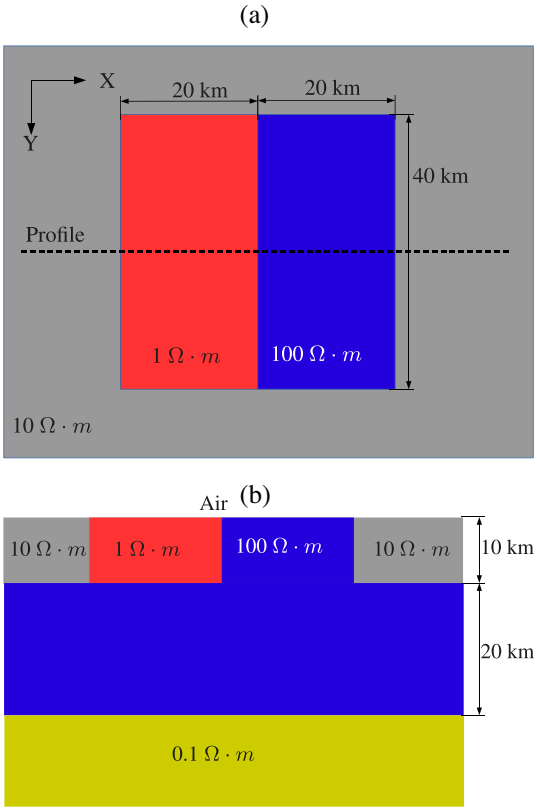

Figure 3. COMMEMI3D-2 model. Top (a)—a plan view of the model and bottom (b)—side view. Dashed line in the top plot depicts the profile along which MT responses are shown in Figs 4 and 5.

2.1 Outline of Galerkin method

Let us assume, that $M \in \Omega$ and rewrite eq. (2) in the following operator form

$$(\mathrm{I} - \mathrm{G_E}\,\Delta_\sigma)\mathbf{E} = \mathbf{E}^b, \tag{5}$$

where $\mathrm{G_E}$ is the integral operator from eq. (2) and I is the identity operator. To solve eq. (5), we use the Galerkin method (Delves & Mohamed 1985; Farquharson & Oldenburg 2002; Zhdanov 2002) which is sketched below.

Let $\mathcal{L}_2[\Omega]$ be a vector Hilbert functional space with the following dot product and norm

$$\begin{aligned}(\mathbf{V}, \mathbf{U}) = \int_\Omega \big(&V_x(M)\overline{U}_x(M) + V_y(M)\overline{U}_y(M) \\ &+ V_z(M)\overline{U}_z(M)\big)\, d\Omega_M, \\ \|\mathbf{V}\| = \sqrt{(\mathbf{V}, \mathbf{V})}.&\end{aligned} \tag{6}$$

Here, the overline above **U** components denotes their complex conjugates.

Let us also assume that vector functions $\mathbf{\Psi}_n$, $n = 1, \ldots, N$ form the orthonormal basis in $\mathcal{L}_2[\Omega]$, denote $\mathcal{Q}^N$ as the linear span of this basis, and define projection operator $\mathbf{P}^{\mathrm{N}}$ from $\mathcal{L}_2[\Omega]$ to $\mathcal{Q}^N$ as follows

$$\begin{aligned}&\mathbf{V}^N = \mathbf{P}^{\mathrm{N}}\mathbf{V} = \sum_{n=1}^{N} a_n \mathbf{\Psi}_n, \\ &a_n = (\mathbf{V}, \mathbf{\Psi}_n), \\ &\mathbf{V} \in \mathcal{L}_2[\Omega] \quad \mathbf{V}^N \in \mathcal{Q}^N.\end{aligned} \tag{7}$$

By construction $\|\mathbf{P}^{\mathrm{N}}\| = 1$ and $\mathbf{V}^N$ is the best approximation of $\mathbf{V} \in \mathcal{L}_2[\Omega]$ in terms of norm (6).

The Galerkin method as applied to eq. (5) relies on an approximation of **E** inside Ω by a function $\mathbf{U} \in \mathcal{Q}^N$, which satisfies the following N equations

$$((\mathrm{I} - \mathrm{G_E}\,\Delta_\sigma)\,\mathbf{U}, \mathbf{\Psi}_n) = (\mathbf{E}^b, \mathbf{\Psi}_n) \quad n = 1, \ldots, N. \tag{8}$$

Substituting the expansion $\mathbf{U} = \sum_{n=1}^{N} u_n \mathbf{\Psi}_n$ into eq. (8), we obtain the system of linear equations for coefficients u_n

$$u_n - \sum_{m=1}^{N} u_m (\mathrm{G_E}\,\Delta_\sigma \mathbf{\Psi}_m, \mathbf{\Psi}_n) = (\mathbf{E}^b, \mathbf{\Psi}_n). \tag{9}$$

By using the definition of projection operator $\mathbf{P}^{\mathrm{N}}$, we can deduce that function **U** obeys the following operator equation in space $\mathcal{Q}^N$

$$\mathbf{U} - \mathbf{P}^{\mathrm{N}}\,\mathrm{G_E}\,\Delta_\sigma \mathbf{U} = \mathbf{P}^{\mathrm{N}}\,\mathbf{E}^b. \tag{10}$$

Equation (10) has a unique solution in $\mathcal{Q}^N$, and thus the system (9) also has a unique solution (see more details in Appendix A).

The final stage of the method is to substitute **U** instead of **E** into the integrands in eqs (2) and (3) in order to obtain $\tilde{\mathbf{E}}$ and $\tilde{\mathbf{H}}$ at any point $M \in \mathbb{R}^3$

$$\tilde{\mathbf{E}}(M) = \mathbf{E}^b(M) + \int_\Omega \widehat{G}_E(M, M_0)\Delta_\sigma(M_0)\mathbf{U}(M_0)\, d\Omega_{M_0}, \tag{11}$$

$$\tilde{\mathbf{H}}(M) = \mathbf{H}^b(M) + \int_\Omega \widehat{G}_H(M, M_0)\Delta_\sigma(M_0)\mathbf{U}(M_0)\, d\Omega_{M_0}. \tag{12}$$

The approximations (11) and (12) guarantee $\mathrm{div}\,\tilde{\mathbf{H}} = 0$ everywhere by design, irrespective of the choice of basis functions $\mathbf{\Psi}_n$. Moreover, eqs (11) and (12) ensure that the components of $\tilde{\mathbf{E}}$ and $\tilde{\mathbf{H}}$ tangential to any plane are continuous across this plane.

2.2 Construction of basis functions

It can be shown (see Appendix B) that for **E**, $\tilde{\mathbf{E}}$, **H** and $\tilde{\mathbf{H}}$ the following inequalities hold

$$\begin{aligned}&|\tilde{\mathbf{E}}(M) - \mathbf{E}(M)| \le C_E^{\mathrm{out}}(M)\|\mathbf{E} - \mathbf{P}^{\mathrm{N}}\mathbf{E}\|, \\ &|\tilde{\mathbf{H}}(M) - \mathbf{H}(M)| \le C_H^{\mathrm{out}}(M)\|\mathbf{E} - \mathbf{P}^{\mathrm{N}}\mathbf{E}\|,\end{aligned} \tag{13}$$

for $M \notin \Omega$ and

$$\begin{aligned}&\|\tilde{\mathbf{E}} - \mathbf{E}\| \le C_E^{\mathrm{in}}\|\mathbf{E} - \mathbf{P}^{\mathrm{N}}\mathbf{E}\|, \\ &\|\tilde{\mathbf{H}} - \mathbf{H}\| \le C_H^{\mathrm{in}}\|\mathbf{E} - \mathbf{P}^{\mathrm{N}}\mathbf{E}\|,\end{aligned} \tag{14}$$

for $M \in \Omega$. Here, $C_{E,H}^{\mathrm{out}}(M)$ are bounded functions and C_E^{in}, C_H^{in} are constants, which are all independent of the basis functions $\mathbf{\Psi}_n$.

The inequalities (13) and (14) demonstrate rather the obvious but important fact that the accuracy of the numerical solution depends on $\|\mathbf{E} - \mathbf{P}^{\mathrm{N}}\mathbf{E}\|$, that is, how well the true electric field **E** is approximated by its projection to $\mathcal{Q}^N$. An optimal choice of space $\mathcal{Q}^N$ is a non-trivial problem, but the insight gained in the FE modeling community (Schwarzbach *et al.* 2011; Grayver & Kolev 2015) promotes the idea to use piecewise polynomial approximation of the electric field.

The estimates above are based on properties of the solution, without considering efforts to calculate coefficients for system (9) quickly and accurately. Such a calculation is the main challenge in any IE approach, even for the PWC basis, where these coefficients are double volumetric integrals of Green's tensors components (Kruglyakov & Bloshanskaya 2017). Note that the first attempt in the EM geophysical community to use the basis different

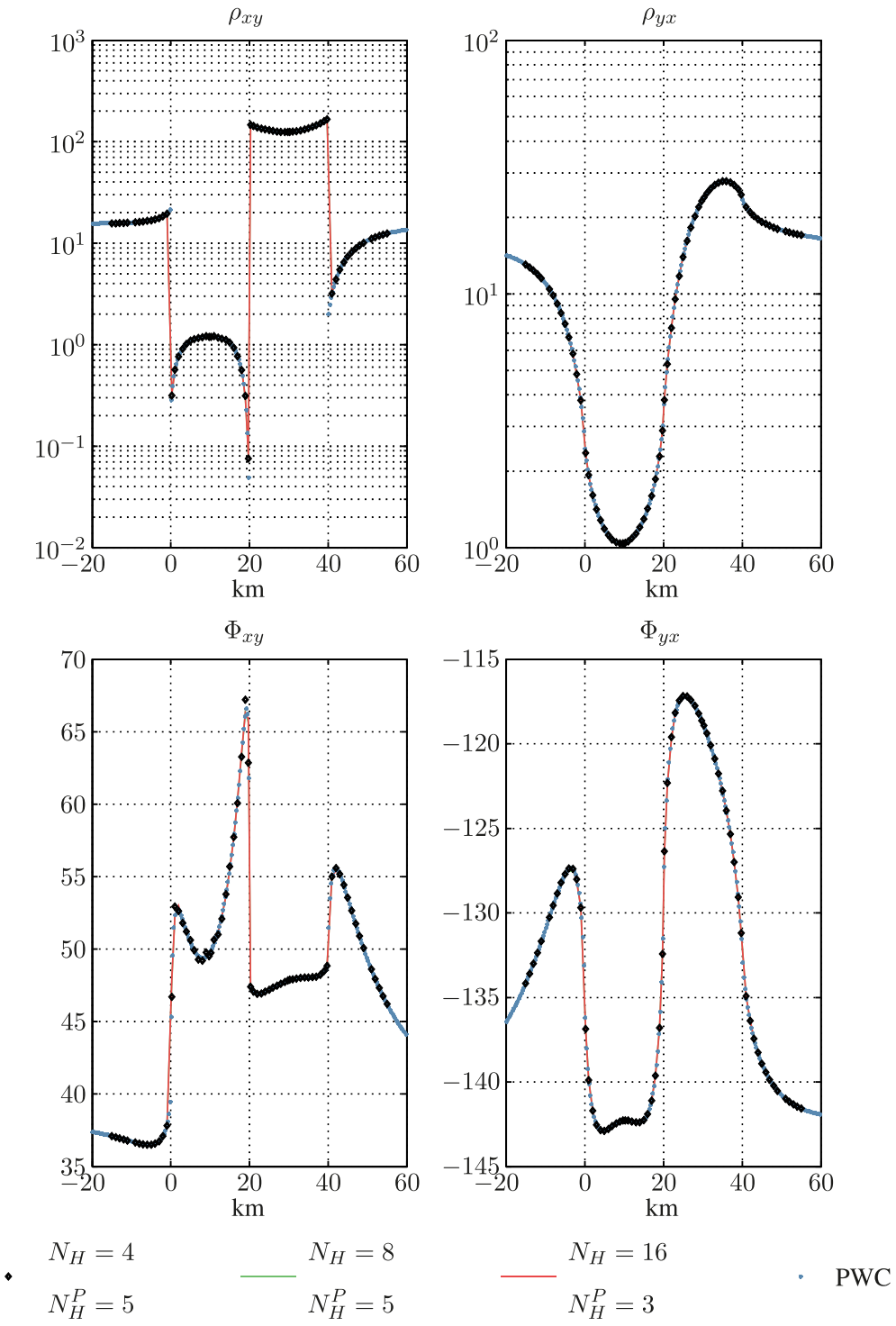

Figure 4. Apparent resistivities and phases along the profile shown by the dashed line in Fig. 3(a). Period is 100 s.

from PWC was undertaken by Farquharson & Oldenburg (2002) who used trilinear approximation. However, the challenge to construct matrix coefficients for this basis compelled authors to use a Green's tensor for the simplest background conductivity model, namely homogeneous space.

In this paper, the calculation of the coefficients for the HOP basis is based on a generalization of the method proposed in Kruglyakov & Bloshanskaya (2017). Taking into account that the partial sum of Fourier–Legendre series provides the best polynomial approximation in $\mathcal{L}_2[-1, 1]$, we made an influential decision to use Legendre-type polynomials. Note, that in general, one can use basis functions from a wide class of Jacobi polynomials, but this implies the usage of weighting functions in dot products $(\mathrm{G_E}\,\Delta_\sigma \Psi_m, \Psi_n)$, which enormously complicates calculation of the matrix coefficients.

The modeling domain Ω is split into $N_c = N_x N_y N_z$ non-overlapping rectangular cells $\bigcup_{n=1}^{N_c} \Omega_n = \Omega$; $N_{x,y,z}$ is the number of cells in the x-, y- and z-directions, respectively, and conductivities

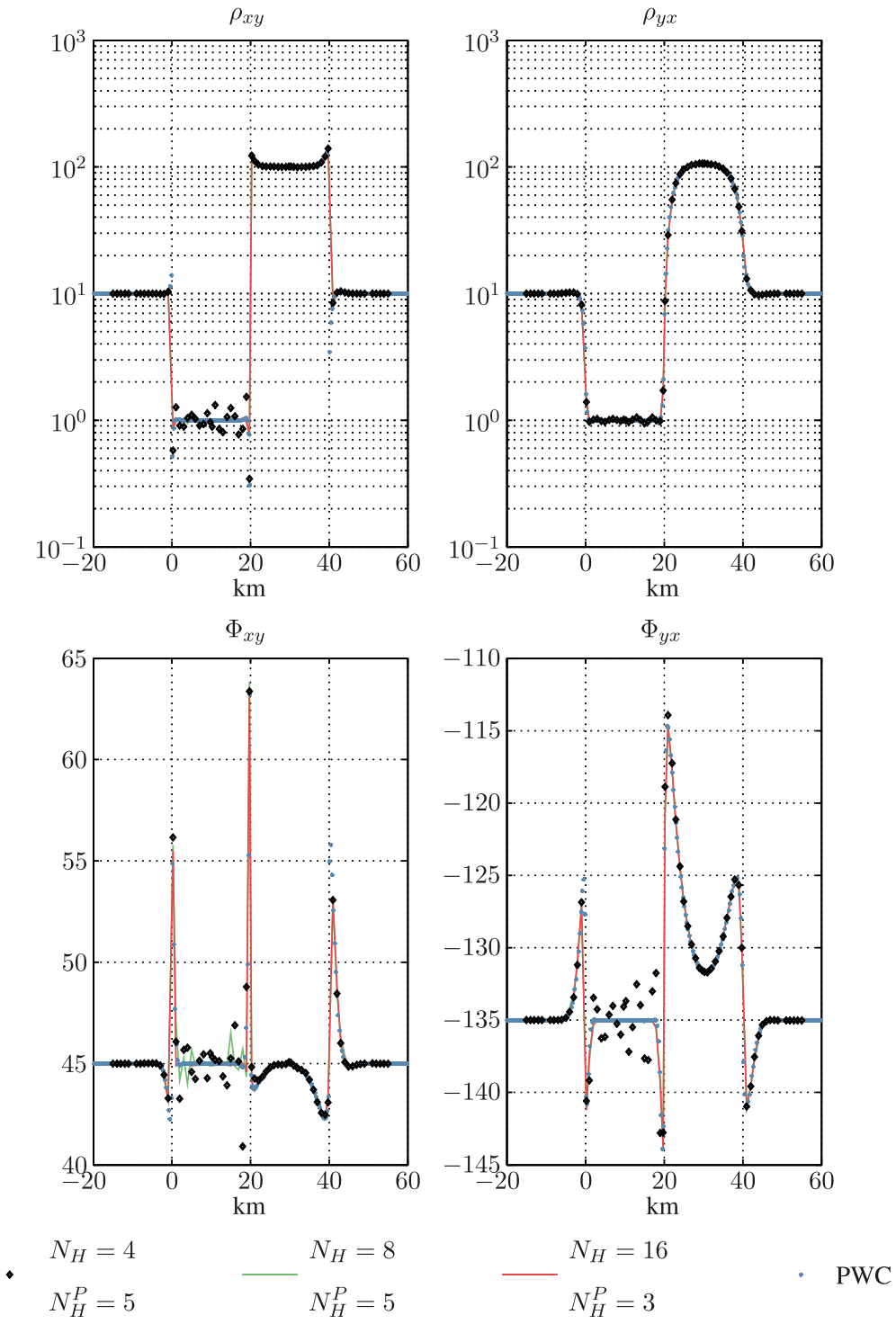

Figure 5. The same legend as in Fig. 4. Period is 1 s.

$\sigma_{a,b}$ are constant inside each cell. For every cell Ω_n the finite scalar basis functions $\Psi_n^{n_x,n_y,n_z}(x, y, z)$ are introduced as follows

$$\Psi_n^{n_x,n_y,n_z}(x,y,z) = \frac{2\sqrt{2}}{\sqrt{h_x h_y h_z}} L_{n_x}\left(2\frac{x-x^n}{h_x^n} - 1\right) \times L_{n_y}\left(2\frac{y-y^n}{h_y^n} - 1\right) \times L_{n_z}\left(2\frac{z-z^n}{h_z^n} - 1\right) \quad (15)$$

where, L_m is the normalized Legendre polynomial of the mth order, h_x^n, h_y^n and h_z^n are the sizes of Ω_n in x, y and z dimensions, and x^n, y^n and z^n are the coordinates of a corner of Ω_n, $n_{x,y,z} = 0, \ldots, N_{x,y,z}^P$, and $N_{x,y,z}^P$ is the maximum polynomial order along the x-, y- and z-directions. Note, that $\Psi_n^{n_x,n_y,n_z} = 0$ outside of Ω_n, $n = 1, \ldots, N_c$.

The vector basis functions $\mathbf{\Psi}_n$, $n = 1, \ldots, N$, $N = 3N_c\left(N_x^P + 1\right)\left(N_y^P + 1\right)\left(N_z^P + 1\right)$ are constructed as $\mathbf{\Psi} = (\Psi_x, \Psi_y, \Psi_z)$, where $\Psi_{x,y,z}$ are those of $\Psi_n^{n_x,n_y,n_z}$.

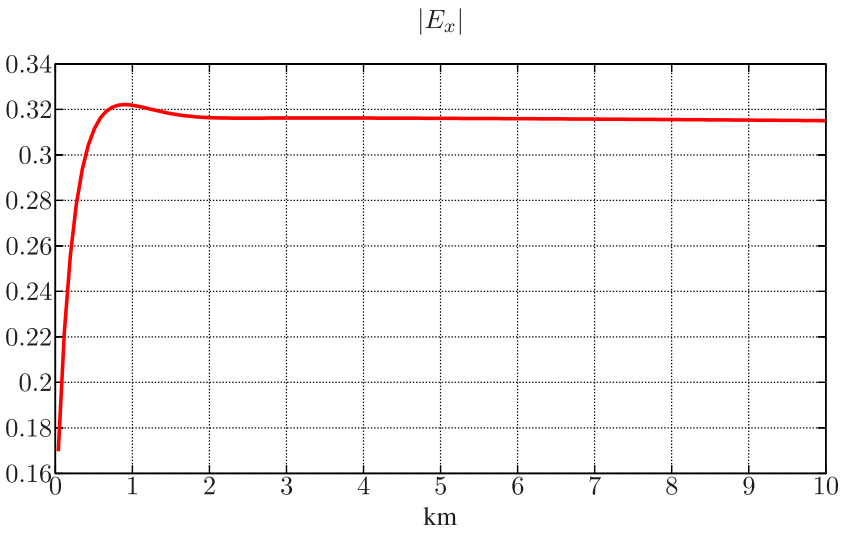

Figure 6. Magnitude of E_x for x-polarization excitation at $z = 0$ along the discussed profile over the left half of the conductive block in the COMMEMI3D-2 model at a period of 1 s.

Table 2. Details of successful modeling runs with HOP and PWC IE solvers for the COMMEMI3D-2 model. N_H stands for a number of cells in every lateral direction. N_H^P is the polynomial order used in the lateral direction. Time is that required for modeling two polarizations.

Run with	N_H	N_H^P	Number of unknowns	RAM (GB)	Time (CPU × s)
HOP (100 s)	4	5	27 648	1.5	195
HOP (1 s)	16	3	196 608	3.5	714
PWC	128		2457 600	10	1260

The orthonormality of $\boldsymbol{\Psi}_n$ follows from the orthonormality of (normalized) Legendre polynomials.

In the terminology of FE, we use the discontinuous Galerkin method, with basis functions that do not guarantee continuity of $\mathbf{U}$ at Ω_n boundaries. However, the continuity of tangential components of $\tilde{\mathbf{E}}$ and $\tilde{\mathbf{H}}$ across the cells' boundaries is secured by eqs (11) and (12), as well as zero divergence of $\tilde{\mathbf{H}}$.

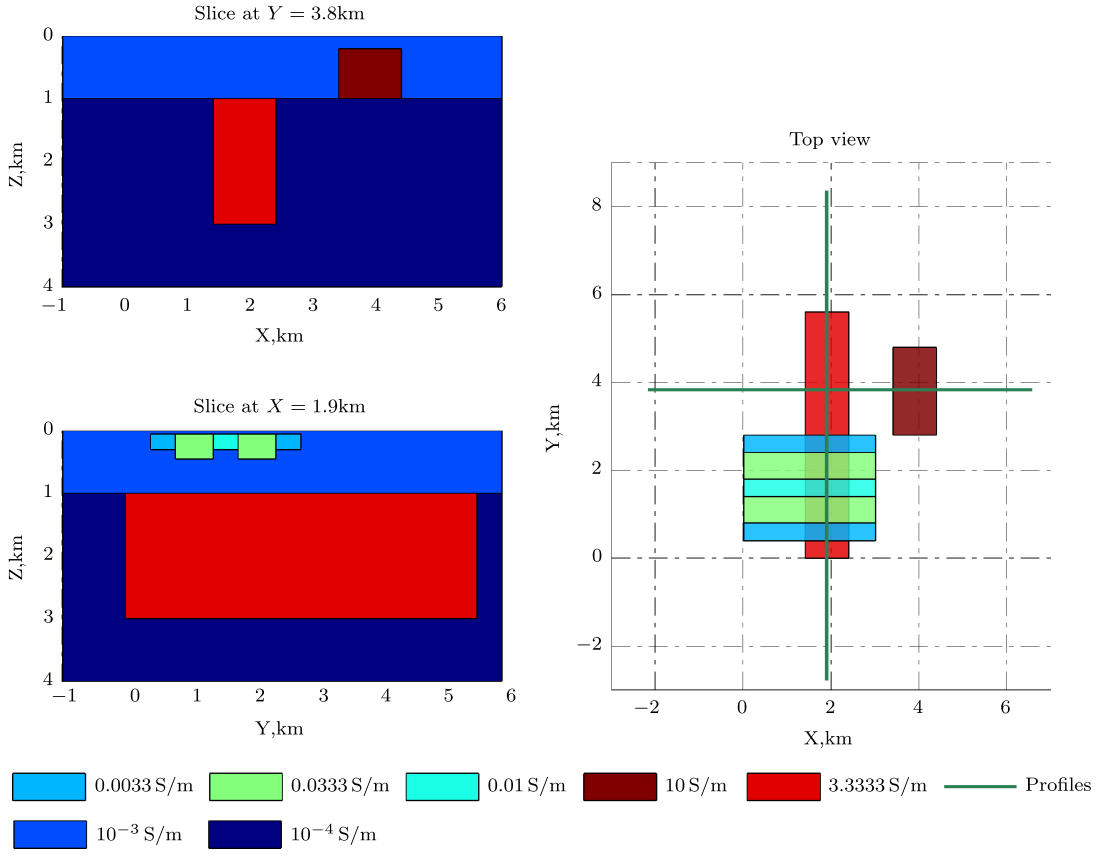

Figure 7. COMMEMI3D-3 model. Left-hand plots show side views of the model and right-hand plots show the plane view.

Table 3. Details of modeling runs for COMMEMI3D-3 model with HOP and PWC IE solvers. N_H^P and N_z^P stand for polynomial orders used in lateral and vertical directions, respectively.

Legend	Run with	Discretization	N_H^P	N_z^P	Number of unknowns
PWC coarse	PWC	$h_x = h_y = 100$ m, h_z from 25 to 250 m			177 408
PWC fine	PWC	$h_x = h_y = h_z = 12.5$ m			111648 768
PWC best	PWC	$h_x = h_y = h_z = 6.25$ m			893190 144
HOP $N_H^P = 1$	HOP	$h_x = h_y = 200$ m, h_z from 10^2 to 10^3 m	1	3	177 408
HOP $N_H^P = 2$	HOP	$h_x = h_y = 200$ m, h_z from 10^2 to 10^3 m	2	3	399 168

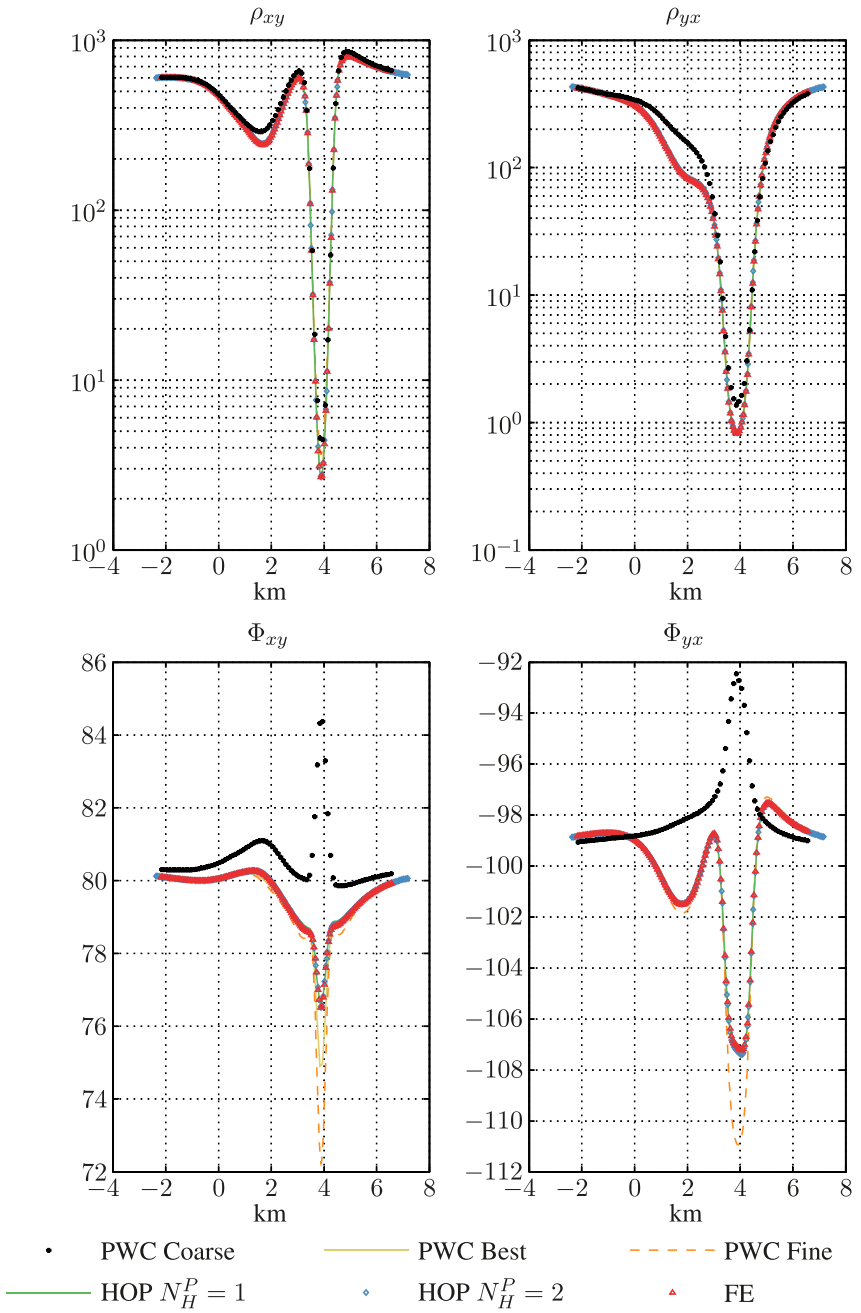

Figure 8. Apparent resistivities ρ_{xy}, ρ_{yx} (above) and impedance phases φ_{xy}, φ_{yx} (below) along the profile $y = 3830$. Period is 1 s.

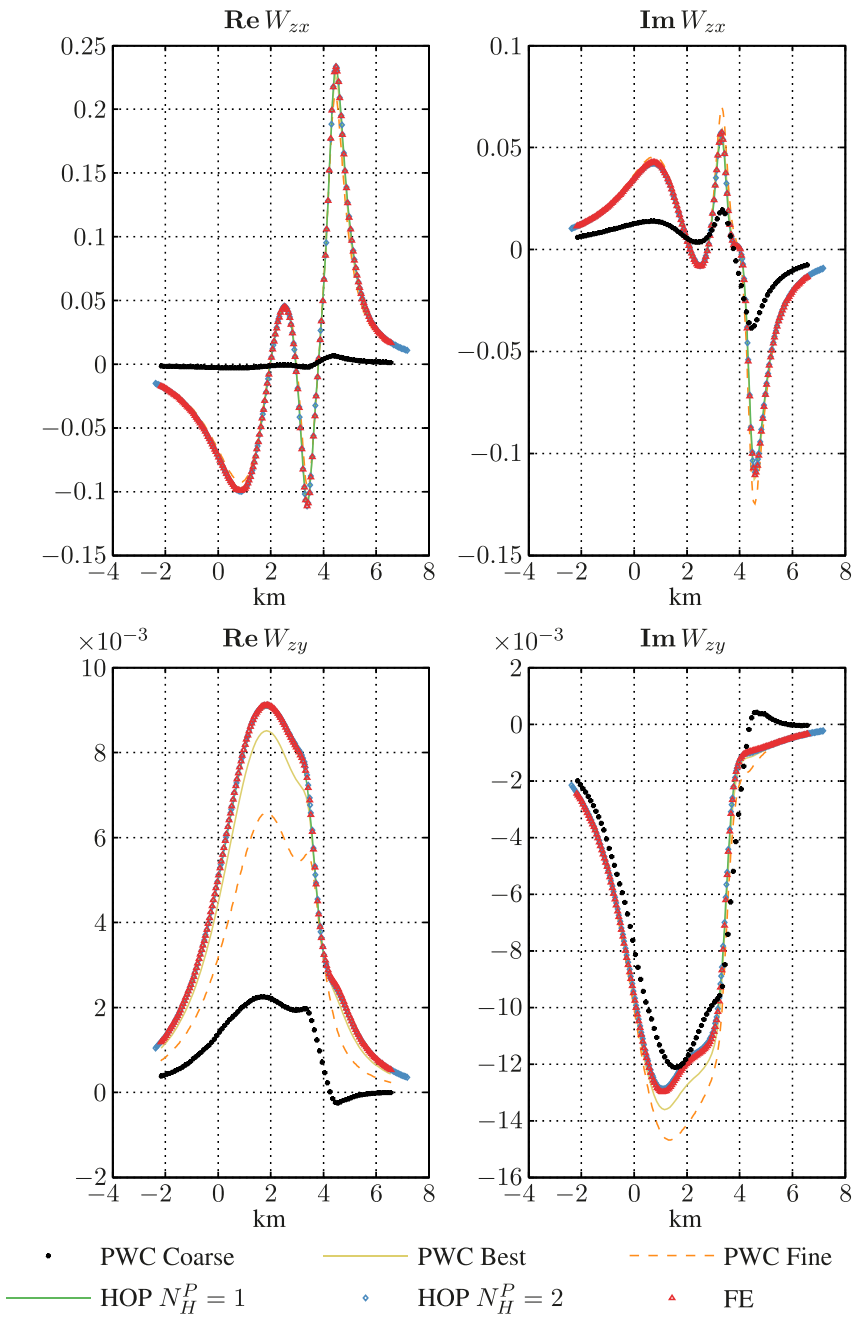

Figure 9. Real (left) and imaginary (right) parts of tippers component W_{xz}, W_{yz} along the profile $y = 3830$. Period is 1 s.

3 CONVERGENCE RATE OF THE METHOD

The inequalities (13) and (14) are formulated in terms of $\left\|\mathbf{E} - \mathbf{P}^{\mathrm{N}}\,\mathbf{E}\right\|$. We can make a step further and estimate $\left\|\mathbf{E} - \mathbf{P}^{\mathrm{N}}\,\mathbf{E}\right\|$ in terms of the maximum cell diameter d and the minimum polynomial order $N^P = \min\{N_x^P, N_y^P, N_z^P\}$

$$\left\|\mathbf{E} - \mathbf{P}^{\mathrm{N}}\,\mathbf{E}\right\|_{\mathcal{L}_2[\Omega]} \leq A d^{N^P+1}, \tag{16}$$

where A is a constant independent of d (but dependent on N^P and $\mathbf{E}$). This result is a corollary from the Bramble–Hilbert lemma (Brenner & Scott 2008), if one recalls that $\mathbf{P}^{\mathrm{N}}\,\mathbf{E}$ is the best polynomial approximation in $\mathcal{L}_2[\Omega_n]$ by design.

Substituting inequality (16) into the right-hand side of inequalities (13) and (14), we obtain that for the fixed polynomial order N^P the method converges with $N^P + 1$ order.

4 REMARKS ON IMPLEMENTATION

The main challenges of any IE-based solver are computation of matrix coefficients [see eq. (9)] and (dense) matrix handling. These challenges have been addressed by using the approaches introduced by Kruglyakov & Bloshanskaya (2017). More specifically, the integrals in the vertical direction are computed analytically by generalization of the approach of Kruglyakov & Bloshanskaya (2017, appendix B), whereas for the horizontal integration special digital filters are constructed (appendix C of the same paper). However,

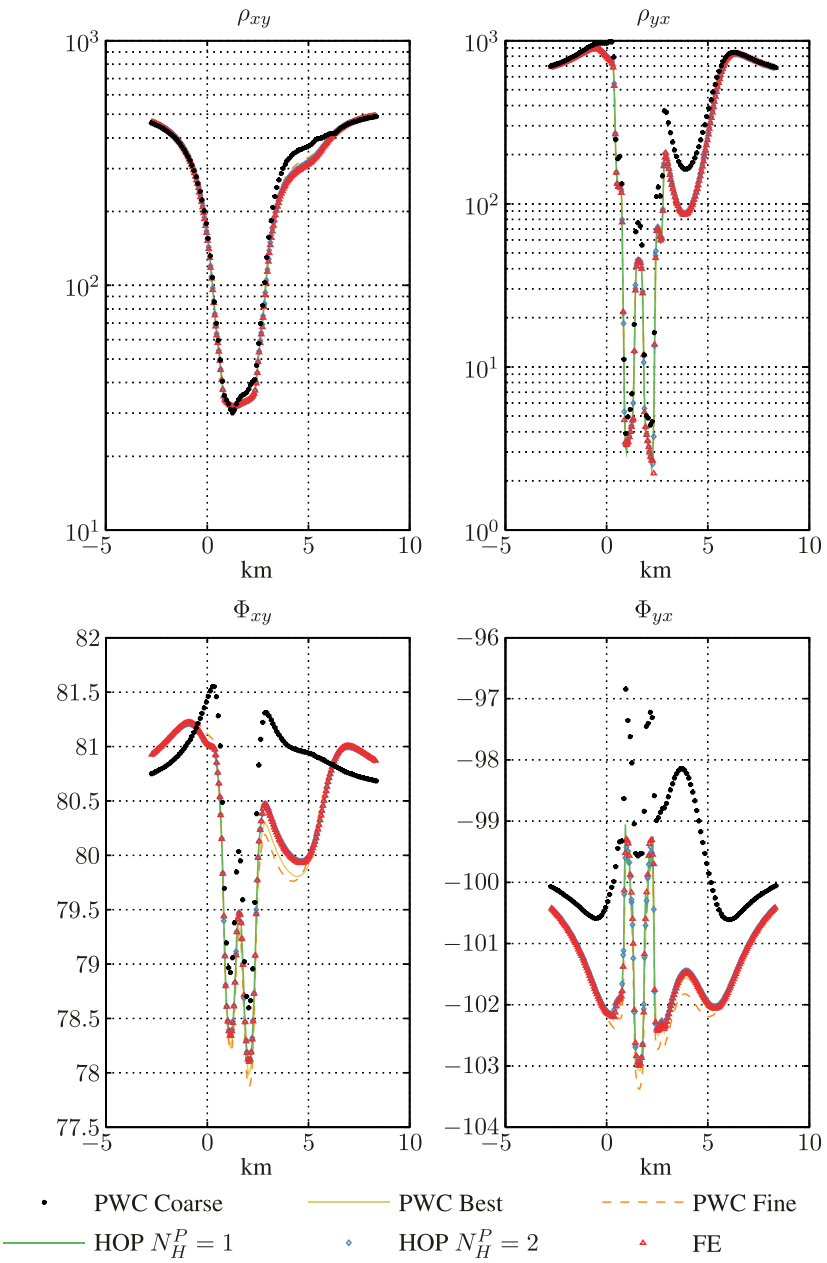

Figure 10. Apparent resistivities ρ_{xy}, ρ_{yx} (above) and impedance phases φ_{xy}, φ_{yx} (below) along the profile $x = 1900$. Period is 1 s.

the analytical transformations involved at these stages are extremely complex and we used the computer algebra system Maxima (2017) to obtain the correct expressions and to generate proper Fortran code.

A standard IE numerical scheme is invoked, based on a uniform discretization in lateral directions. It yields a block-Toeplitz system matrix, thus decreasing memory requirements and accelerating matrix-vector multiplication by using a 2-D fast Fourier transform (*cf.* Avdeev *et al.* 1997). In addition, system matrix symmetries and antisymmetries were utilized to further reduce computational and memory loads as in Kruglyakov & Bloshanskaya (2017).

Finally, the resulting system of equations is solved by Krylov subspace iterations using our own implementation of the FGMRES method (Saad 1993). To obtain faster convergence to the solution, we use IE with a contracting kernel approach (Singer 1995; Pankratov *et al.* 1995; Zhdanov 2002), hereinafter denoted as contracting IE (CIE). The advantage of using CIE is that the condition number of the CIE system matrix depends only on the lateral conductivity contrast (*cf.* Pankratov & Kuvshinov 2016), which permits use of the HOP method without additional preconditioning of the system matrix. The only reason we use conventional IE in the equations above is to simplify the explanation.

5 NUMERICAL EXPERIMENTS

To explore the performance of the HOP IE-based solver against the one which uses PWC basis functions, we performed simulations of magnetotelluric (MT) responses using three different models of 3-D conductivity distribution.

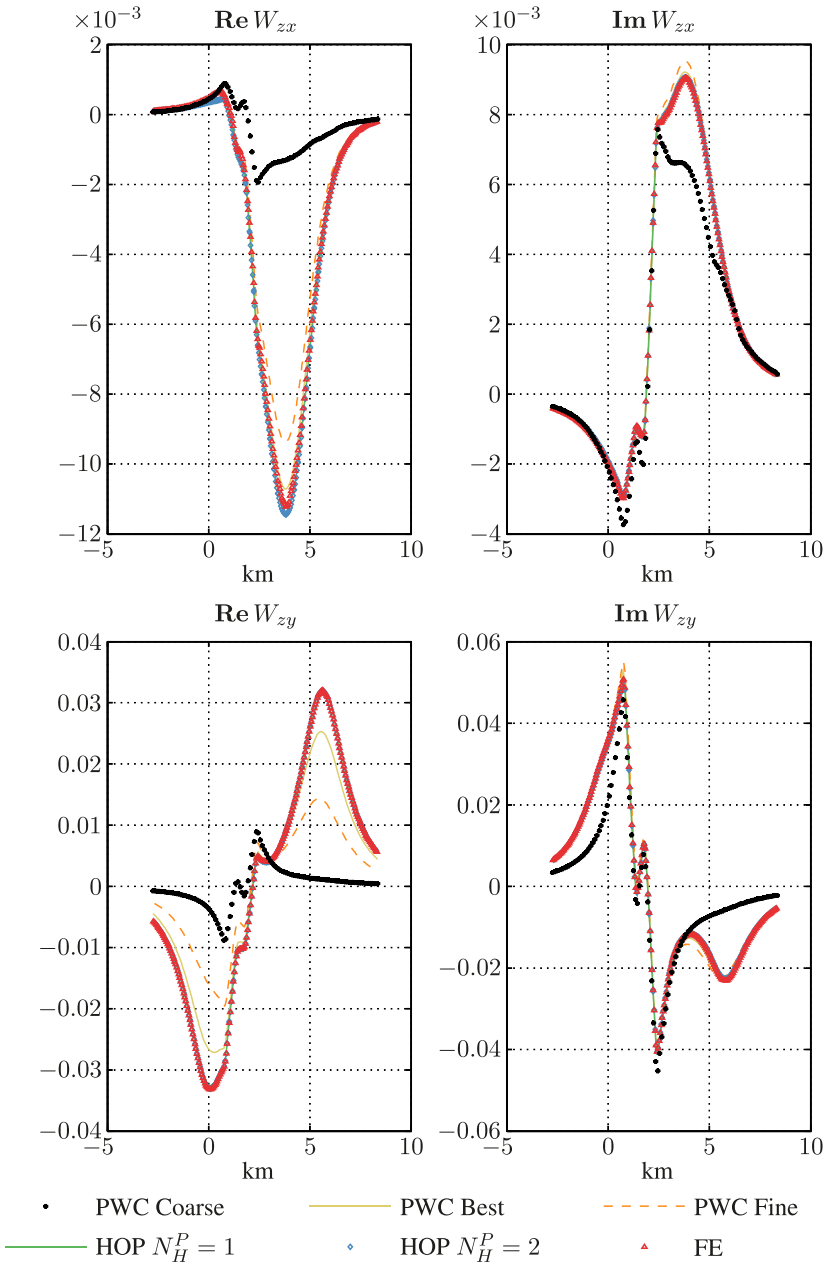

Figure 11. Real (left) and imaginary (right) parts of tippers component W_{xz}, W_{yz} along the profile $x = 1900$. Period is 1 s.

5.1 Fault model

We start with presenting results for a case in which polynomials are implemented along the vertical direction only. The model taken from Bakker *et al.* (2015) mimics a conducting sedimentary basin surrounded by resistive mountains with a conductive fault beneath the left flank of the basin. Plane and side views of the model are shown in the respective upper and lower plots in Fig. 1. We expect galvanic coupling between the high-conductive sedimentary basin and the deep conducting basement by the downward leakage of electric currents within the fault, thus assuming that accurate approximation of the electric field in the vertical direction is essential.

The need for accurate approximation is clearly seen in Fig. 2, where the modeling by a PWC IE solver with vertical discretization $N_z = 32$ produces an artefact at the right flank of the fault. Increasing N_z in the course of PWC modeling improves the results, as expected. The artefact disappears when rather excessive discretization with $N_z = 128$ is invoked. Remarkably, the usage of a third-order polynomial basis in the vertical direction gives accurate results already with $N_z = 2$. Note that lateral discretization $h_x = h_y = 200$ m was used for all runs, for both PWC and HOP modeling. Details of the successful runs are summarized in Table 1. It is evident from the table that in order to reach the same accuracy one needs 16 times fewer unknowns if the HOP solver is invoked. In terms of computational loads the gains are 25 and 8 for the memory and time, respectively.

5.2 Two block (COMMEMI3D-2) model

The developed HOP IE solver permits the use of polynomials up to fifth order in all directions. In this section, we explore the

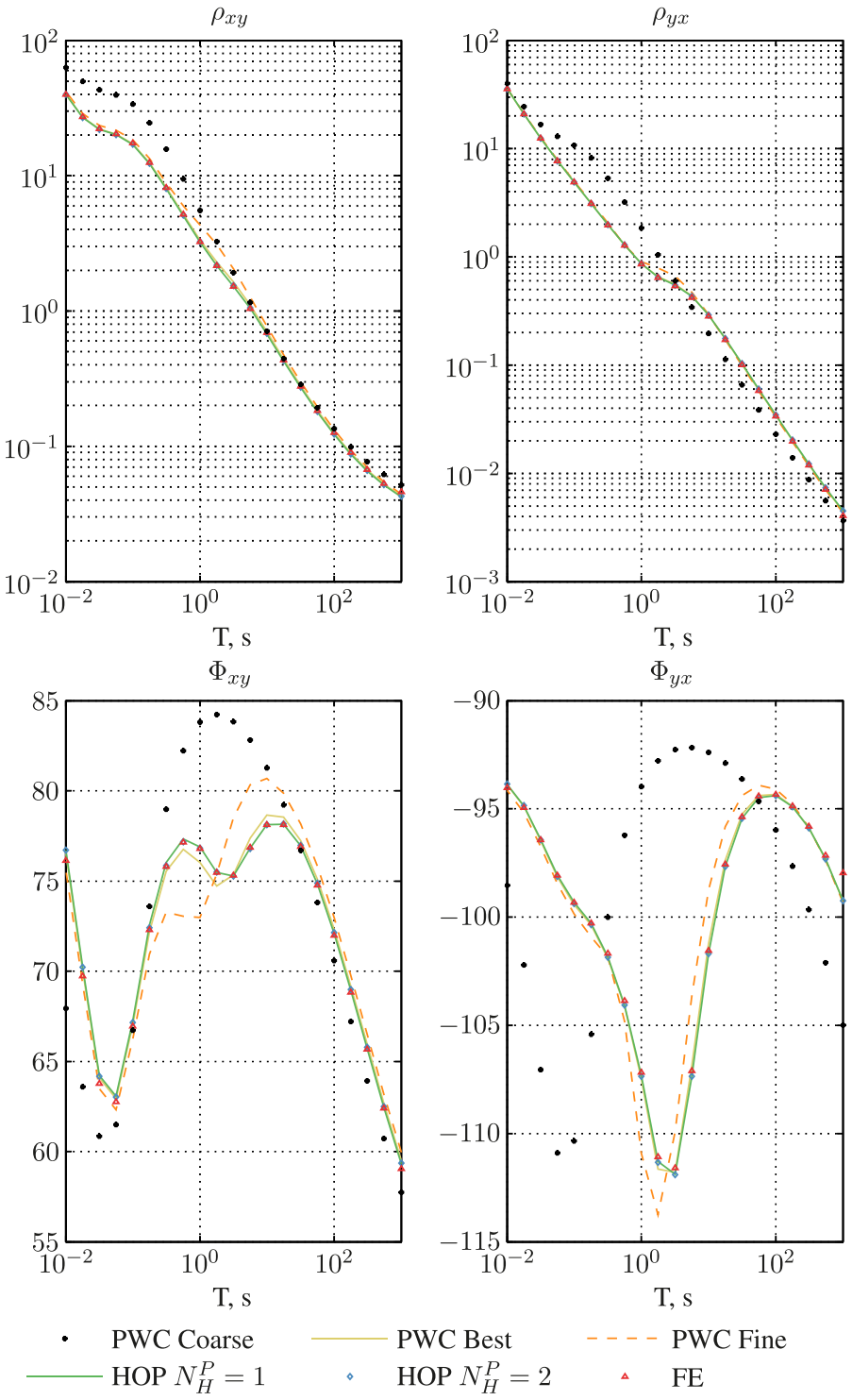

Figure 12. Apparent resistivities ρ_{xy}, ρ_{yx} (above) and impedance phases φ_{xy}, φ_{yx} (below) with respect to period at point (3975, 3830).

interplay between the order of polynomials in a lateral direction and lateral discretization of the model. Modelings were performed using the COMMEMI3D-2 model from Zhdanov *et al.* (1997) (see Fig. 3) in the period range between 1 and 100 s. In all HOP simulations, we use third-order polynomials in the vertical direction and $N_z = 4$ with vertical cell sizes of 500, 500, 4000 and 5000 m. In the course of HOP simulations, the following combinations of lateral discretization of the model, N_H, and order of polynomials in the lateral direction, N_H^P, were tried: $N_H = 4$, $N_H^P = 5$; $N_H = 8$, $N_H^P = 5$ and $N_H = 16$, $N_H^P = 3$. For all PWC simulations, $N_H = 128$ and $N_z = 50$ with vertical cell sizes growing in geometric sequence from 10 to 845 m. Numerical experiments (not shown here) demonstrate that this combination of N_H and N_z provides accurate PWC results for all considered periods.

The numerical simulations also show that the efficiency of HOP may depend on the period. At a period of 100 s (Fig. 4), the

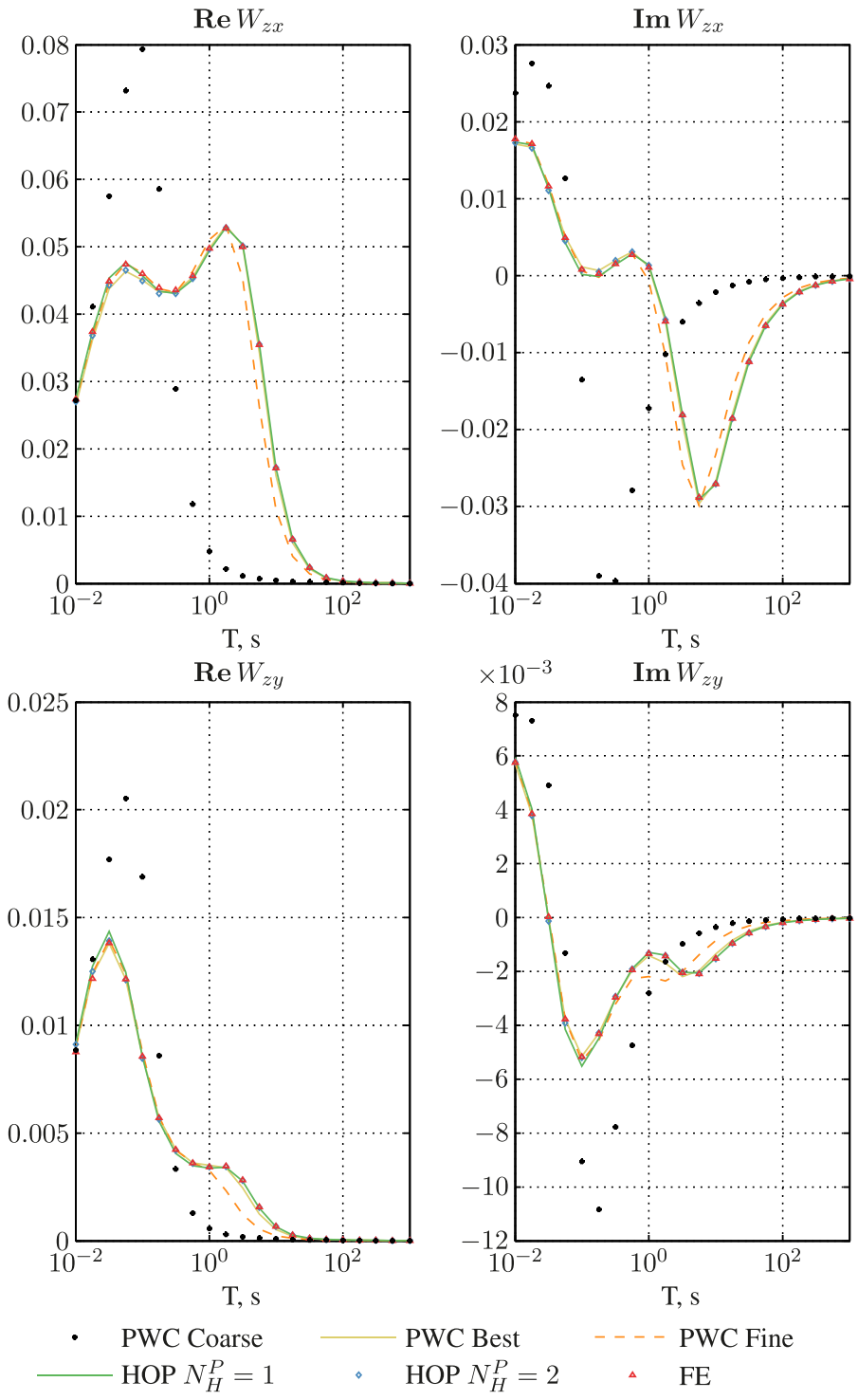

Figure 13. Real (left) and imaginary (right) parts of tippers component W_{xz}, W_{yz} (below) with respect to period at point (3975, 3830).

electric field inside a cell is rather smooth and the HOP approach yields accurate results using a very coarse lateral grid (two cells per block) provided fifth-order polynomials are used. At the same time, the PWC solver requires 128 cells in a lateral direction to obtain results of comparable accuracy. Cumulatively, for a period of 100 s, by using the HOP solver one needs 100 times fewer unknowns to obtain accurate results, and the corresponding gains in terms of computational loads are 6 and 7 for the memory and time, respectively.

At a period of 1 s, accurate results by the HOP are obtained for the combination $N_H = 16$, $N_H^P = 3$ meaning that a denser lateral grid is used (Fig. 5). At this period, the electric field varies sharply inside the conductive block (Fig. 6) and thus the lateral cell's size has to be decreased (which is what we did) or the polynomial order has to be significantly increased.

Despite a denser lateral grid for this period ($N_H = 16$), the HOP solver still outperforms PWC solver, but the gain is smaller (3 and 1.8 for the memory and time) than for 100 s modeling. However,

Table 4. Details of successful modeling runs for COMMEMI3D-3 model with HOP and PWC IE solvers. Time is for modeling two polarizations.

Legend	Number of unknowns	RAM (GB)	Time (CPU × hours)
PWC best	893190 144	10 000	4500
HOP $N_H^P = 1$	177 408	2.81	0.8

we note here that the HOP performance can be improved by using non-regular lateral grids, which is the subject of further research. Details of successful HOP and PWC modeling runs are summarized in Table 2.

5.3 Large conductivity contrast (COMMEMI3D-3) model

An accurate computation of electric and magnetic fields in media with a large conductivity contrast is one of the most challenging problems of EM modeling. This is due to strong interconnection between the lateral conductivity contrast and the matrix condition number (Pankratov & Kuvshinov 2016). The large conductivity contrast COMMEMI3D-3 model (Hursan & Zhdanov 2002; Varentsov *et al.* 2000) is considered as the third test model for the presented solver. This model schematically describes the conductivity distribution typical for ore exploration with MT.

The COMMEMI3D-3 model consists of seven rectangular blocks embedded in a layered medium (Fig. 7). The background section of the model consists of two layers with conductivities of 10^{-3}, 10^{-4} S m^{-1}, and a lower half-space with conductivity of 0.1 S m^{-1}. The thicknesses of the first and the second layers are 1 and 6.5 km, respectively. The maximum lateral conductivity contrast is 10^4 in the first layer and 3.3×10^4 in the second layer.

The MT responses were calculated along two representative profiles (Fig. 7) in a period range between 0.01 and 1000 s using different discretizations and polynomial orders (*cf.* Table 3). The IE modeled responses (Figs 8–13) were compared with those from the reference second-order FE solver by Grayver & Kolev (2015).

In all figures, one observes excellent agreement between the HOP IE and the FE solvers. Note that this agreement is achieved with the HOP IE solver by using a very moderate number (around 2×10^5) of unknowns, with bilinear basis in lateral directions and cubic basis in the vertical direction. Note that the increasing polynomial order in lateral directions practically does not change the results.

Interestingly, when the HOP solver is used, a rather coarse lateral grid (with $h_x = h_y = 200$ m) is sufficient for accurate modeling of the responses over the shallow structure. It is quite unexpected, because the electric field varies non-negligibly inside shallow blocks and their sizes in the y-direction (from 400 to 600 m) are comparable with the cell sizes (Figs 10–11).

At the same time, using the PWC IE solver requires around 9×10^8 unknowns to obtain results of comparable accuracy, which leads to a corresponding difference in computational loads (*cf.* Table 4). A coarser discretization does not produce 'true' results in apparent resistivity over the conductive block at periods from 0.1 to 10 s (upper parts of Figs 8 and 12). Nor does it do so for the phases at any periods (lower parts of Figs 8 and 12). Moreover, even with the 'best' discretization (cubic cells of 6.25 m size), the PWC impedance phases do not perfectly agree with those from the FE and HOP solvers. As a final remark, if PWC and HOP discretizations are comparable (by giving exactly the same number of unknowns), the PWC results differ considerably from the 'true' results, especially above the high-conductive block, and most prominently in phases of impedance and tippers (Figs 8–13).

6 CONCLUDING REMARKS

We present an IE solver which exploits high- (up to fifth) order polynomial basis functions. The solver outperforms IE solvers based on a conventional PWC basis in terms of both memory savings and acceleration of computations due to a decrease in the number of unknowns by one to several orders of magnitude. The gain depends on model and period. In the best scenario presented in the paper, the gain is four orders of magnitude. Such extreme reduction in computational loads opens an avenue for using non-uniform grids in lateral directions which were computationally forbidden in PWC IE solvers. It will allow, in particular, to use the IE approach for large-scale regional modeling where complex local 3-D effects from topography and bathymetry are important.

We applied the solver to an MT problem. The extension of the code on the controlled-source case is rather straightforward and is the topic of ongoing realization. Finally, we note that the presented solver is designed to work in Cartesian geometry. The extension of the concept to a spherical geometry is also the topic of future research.

ACKNOWLEDGEMENTS

The authors thank Alexander Grayver for providing his FE results and William Lowrie for improving the English presentation of this paper. We also extend our gratitude to Michael Zhdanov, Takao Koyama and Joerg Renner for many constructive comments on the manuscript. This work is supported by the Swiss Government Excellence Scholarships for Foreign Scholars, Scholarship no 2016.0049 and the Swiss National Supercomputing Center (CSCS) grant (project ID s767).

REFERENCES

Avdeev, D., Kuvshinov, A., Pankratov, O. & Newman, G., 1997. High-performance three-dimensional electromagnetic modeling using modified Neumann series. Wide-band numerical solution and examples, *J. Geomagn. Geoelectr.,* **49,** 1519–1539.

Avdeev, D., Kuvshinov, A., Pankratov, O. & Newman, G., 2002. Three-dimensional induction logging problems, Part I: an integral equation solution and model comparisons, *Geophysics,* **67**(2), 413–426.

Bakker, J., Kuvshinov, A., Samrock, F., Geraskin, A. & Pankratov, O., 2015. Introducing inter-site phase tensors to suppress galvanic distortion in the telluric method, *Earth Planets Space,* **67**(1), 160, doi:10.1186/s40623-015-0327-7.

Brenner, S. & Scott, L., 2008. *The Mathematical Theory of Finite Element Methods,* Springer New York.

Delves, L. & Mohamed, J., 1985. *Computational Methods for Integral Equations,* Cambridge University Press.

Egbert, G.D. & Kelbert, A., 2012. Computational recipes for electromagnetic inverse problems, *Geophys. J. Int.,* **189**(1), 251–267.

Farquharson, C.G. & Miensopust, M.P., 2011. Three-dimensional finite-element modelling of magnetotelluric data with a divergence correction, *J. appl. Geophys.,* **75,** 699–710.

Farquharson, C.G. & Oldenburg, D.W., 2002. An integral equation solution to the geophysical electromagnetic forward-modelling problem, in *Three-Dimensional Electromagnetics: Methods in Geochemistry and Geophysics,* Vol. 35, pp. 3–19, eds Zhdanov, M.S. & Wannamaker, P.E., Elsevier.

Gilbarg, D. & Trudinger, N., 2001. *Elliptic Partial Differential Equations of Second Order,* Springer, Berlin Heidelberg.

Grayver, A. & Burg, M., 2014. Robust and scalable 3-D geo-electromagnetic modelling approach using the finite element method, *Geophys. J. Int.,* **198,** 110–125.

Grayver, A. & Kolev, T., 2015. Large-scale 3D geo-electromagnetic modeling using parallel adaptive high-order finite element method, *Geophysics,* **80**(6), 277–291.

Haber, E. & Ascher, U.M., 2001. Fast finite volume simulation of 3D electromagnetic problems with highly discontinuous coefficients, *SIAM J. Sci. Comput.,* **22**(6), 1943–1961.

Hursan, G. & Zhdanov, M.S., 2002. Contraction integral equation method in three-dimensional electromagnetic modeling, *Radio Sci.,* **37**(6), 1–13, 1089.

Kamm, J. & Pedersen, L.B., 2014. Inversion of airborne tensor VLF data using integral equations, *Geophys. J. Int.,* **198**(2), 775–794.

Koyama, T., Utada, H. & Avdeev, D., 2008. Fast and memory-saved 3-D forward modeling code for MT by using integral equation method, in *Abstract book,* p. 725, ed. Chinese Geophysical Society, 19th Workshop on Electromagnetic Induction in the Earth, Beijing,China.

Kruglyakov, M. & Bloshanskaya, L., 2017. High-performance parallel solver for integral equations of electromagnetics based on Galerkin method, *Math. Geosci.,* **49**(6), 751–776.

Kruglyakov, M., Geraskin, A. & Kuvshinov, A., 2016. Novel accurate and scalable 3-D MT forward solver based on a contracting integral equation method, *Comput. Geosci.,* **96,** 208–217.

Mackie, R., Smith, J. & Madden, T., 1994. 3-Dimensional electromagnetic modeling using finite-difference equation—the magnetotelluric example, *Radio Sci.,* **29**(4), 923–935.

Maxima, 2017. *Maxima, a Computer Algebra System. Version 5.40*, http://maxima.sourceforge.net/, last access date 28 February 2018.

Newman, G. & Alumbaugh, D., 2002. Three-dimensional induction logging problems, Part 2: a finite-difference solution, *Geophysics,* **61,** 484–491.

Pankratov, O. & Kuvshinov, A., 2016. Applied mathematics in EM studies with special emphasis on an uncertainty quantification and 3-D integral equation modelling, *Surv. Geophys.,* **37**(1), 109–147.

Pankratov, O., Avdeyev, D. & Kuvshinov, A., 1995. Electromagnetic-field scattering in a heterogeneous Earth: a solution to the forward problem, *Izv-Phys. Solid Earth,* **31**(3), 201–209.

Puzyrev, V., Koldan, J., de la Puente, J., Houzeaux, G., Vazquez, M. & Cela, J.M., 2013. A parallel finite-element method for three-dimensional controlled-source electromagnetic forward modelling, *Geophys. J. Int.,* **193,** 678–693.

Ren, Z., Kalscheuer, T. & Greenhalgh, S.Maurer H., 2013. A goal-oriented adaptive finite-element approach for plane wave 3-D electromagnetic modelling, *Geophys. J. Int.,* **194,** 700–718.

Saad, Y., 1993. A flexible inner-outer preconditioned GMRES algorithm, *SIAM J. Sci. Comput.,* **14**(2), 461–469.

Schwarzbach, C., Börner, R.-U. & Spitzer, K., 2011. Three-dimensional adaptive higher order finite element simulation for geo-electromagnetics - a marine CSEM example, *Geophys. J. Int.,* **187,** 63–74.

Singer, B., 1995. Method for solution of Maxwell's equations in non-uniform media, *Geophys J Int,* **120,** 590–598.

Singer, B., 2008. Electromagnetic integral equation approach based on contraction operator and solution optimization in Krylov subspace, *Geophys. J. Int.,* **175,** 857–884.

Um, E.S., Commer, M. & Newman, G.A., 2013. Efficient pre-conditioned iterative solution strategies for the electromagnetic diffusion in the earth: finite-element frequency-domain approach, *Geophys. J. Int.,* **193,** 1460–1473.

Varentsov, I.M., Fomenko, I.Y., Golubev, N.G., Mehanee, S., Hursan, G. & Zhdanov, M.S., 2000. Comparative study of 3-D finite difference and integral equation methods, in *Proceedings of 2000 Consortium for Electromagnetic Modeling and Inversion Annual Meeting,* pp. 35–74, University of Utah, Salt Lake City.

Ward, S.H. & Hohmann, G.W., 1988. *4. Electromagnetic Theory for Geophysical Applications,* chap. 4, pp. 130–311, SEG, USA.

Zhdanov, M., Varentsov, I., Weaver, J., Golubev, N. & Krylov, V., 1997. Methods for modelling electromagnetic fields results from commemi-the international project on the comparison of modelling methods for electromagnetic induction, *J. appl. Geophys.,* **37**(3), 133–271.

Zhdanov, M.S., 2002. Chapter 9 - integral representations in electromagnetic forward modeling, in *Geophysical Inverse Theory and Regularization Problems, Methods in Geochemistry and Geophysics,* Vol. 36, pp. 231–286, ed. Zhdanov, M.S., Elsevier.

APPENDIX A: EXISTENCE AND UNIQUENESS OF THE IE SOLUTION BASED ON GALERKIN METHOD

The simplest way to prove the existence and uniqueness of the solution of eq. (10) is to use the CIE approach. Let us make the natural assumption that $\mathbf{Re}\,\sigma_b(z) > 0$ for $M(x, y, z) \in \Omega$ and define operator $\mathbf{G}_{\mathrm{E}}^{\mathrm{m}}$ as follows

$$\mathbf{G}_{\mathrm{E}}^{\mathrm{m}}\,\mathbf{V} = \sqrt{\mathbf{Re}\,\sigma_b}\,\mathrm{G}_{\mathrm{E}}\left[2\sqrt{\mathbf{Re}\,\sigma_b}\mathbf{V}\right] + \mathbf{V}. \tag{A1}$$

Using eq. (A1), we can express G_{E} as

$$\mathrm{G}_{\mathrm{E}} = \frac{1}{2\sqrt{\mathbf{Re}\,\sigma_b}}\left(\mathbf{G}_{\mathrm{E}}^{\mathrm{m}} - \mathrm{I}\right)\frac{1}{\sqrt{\mathbf{Re}\,\sigma_b}} \tag{A2}$$

and rewrite eq. (10) as

$$\left(\mathrm{I} - \mathbf{P}^{\mathrm{N}}\,\mathbf{G}_{\mathrm{E}}^{\mathrm{m}}\,\frac{b}{a}\right)\tilde{\mathbf{U}} = \sqrt{\mathbf{Re}\,\sigma_b}\mathbf{E}^{N}, \tag{A3}$$

where

$$\tilde{\mathbf{U}} = a\mathbf{U}, \quad a = \frac{\sigma_a + \overline{\sigma_b}}{2\sqrt{\mathbf{Re}\,\sigma_b}} \quad b = \frac{\sigma_a - \sigma_b}{2\sqrt{\mathbf{Re}\,\sigma_b}}. \tag{A4}$$

Taking into account that $\left\|\mathbf{P}^{\mathrm{N}}\right\| = 1$, $\left|\frac{b}{a}\right| < 1$, and $\mathbf{G}_{\mathrm{E}}^{\mathrm{m}}$ is a contracting operator (Pankratov *et al.* 1995; Singer 1995), we can construct $\left(\mathrm{I} - \mathbf{P}^{\mathrm{N}}\,\mathbf{G}_{\mathrm{E}}^{\mathrm{m}}\,\frac{b}{a}\right)^{-1}$ as the following Neumann's series

$$\left(\mathrm{I} - \mathbf{P}^{\mathrm{N}}\,\mathbf{G}_{\mathrm{E}}^{\mathrm{m}}\,\frac{b}{a}\right)^{-1} = \sum_{n=0}^{\infty}\left(\mathbf{P}^{\mathrm{N}}\,\mathbf{G}_{\mathrm{E}}^{\mathrm{m}}\,\frac{b}{a}\right)^{n}. \tag{A5}$$

Using eq. (A5), we obtain

$$\left\|\left(\mathrm{I} - \mathbf{P}^{\mathrm{N}}\,\mathbf{G}_{\mathrm{E}}^{\mathrm{m}}\,\frac{b}{a}\right)^{-1}\right\| \leq \sum_{n=0}^{\infty}\left\|\mathbf{P}^{\mathrm{N}}\,\mathbf{G}_{\mathrm{E}}^{\mathrm{m}}\,\frac{b}{a}\right\|^{n}. \tag{A6}$$

Hence, using definitions (A4), and taking into account that $\left|\frac{\sigma_a - \sigma_b}{\sigma_a + \overline{\sigma_b}}\right| < 1$ [*cf.* Pankratov & Kuvshinov (2016)] gives

$$\sum_{n=0}^{\infty}\left\|\mathbf{P}^{\mathrm{N}}\,\mathbf{G}_{\mathrm{E}}^{\mathrm{m}}\,\frac{b}{a}\right\|^{n} \leq \sum_{n=0}^{\infty}\left(\max_{\Omega}\left|\frac{\sigma_a - \sigma_b}{\sigma_a + \overline{\sigma_b}}\right|\right)^{n} = \frac{1}{1 - \max\limits_{\Omega}\left|\frac{\sigma_a - \sigma_b}{\sigma_a + \overline{\sigma_b}}\right|}. \tag{A7}$$

Using eq. (A1) to express G_{E} in terms of $\mathbf{G}_{\mathrm{E}}^{\mathrm{m}}$, we have

$$\left(\mathrm{I} - \mathbf{P}^{\mathrm{N}}\,\mathrm{G}_{\mathrm{E}}\,\Delta_\sigma\right)^{-1} = 2\frac{\sqrt{\mathbf{Re}\,\sigma_b}}{\sigma_a + \overline{\sigma_b}}\left(\mathrm{I} - \mathbf{P}^{\mathrm{N}}\,\mathbf{G}_{\mathrm{E}}^{\mathrm{m}}\,\frac{b}{a}\right)^{-1}\sqrt{\mathbf{Re}\,\sigma_b}. \tag{A8}$$

Thus, we conclude that operator $\left(\mathrm{I} - \mathbf{P}^{\mathrm{N}}\,\mathrm{G}_{\mathrm{E}}\,\Delta_\sigma\right)^{-1}$ is bounded

$$\left\|\left(\mathrm{I} - \mathbf{P}^{\mathrm{N}}\,\mathrm{G}_{\mathrm{E}}\,\Delta_\sigma\right)^{-1}\right\| \leq S = 2\max_{\Omega}\frac{\sqrt{\mathbf{Re}\,\sigma_b}}{|\sigma_a + \overline{\sigma_b}|}\frac{\max\limits_{\Omega}\sqrt{\mathbf{Re}\,\sigma_b}}{1 - \max\limits_{\Omega}\left|\frac{\sigma_a - \sigma_b}{\sigma_a + \overline{\sigma_b}}\right|}. \tag{A9}$$

and consequently eq. (10) has a unique solution.

APPENDIX B: OBTAINING INEQUALITIES OF SECTION 2.2

To obtain error estimations for the proposed method, let us rewrite eqs (5), (10) and (11) in the following operator form

$$\mathbf{E} - \mathrm{G_E}\,\Delta_\sigma \mathbf{E} = \mathbf{E}^b, \tag{B1}$$

$$\tilde{\mathbf{E}} - \mathrm{G_E}\,\Delta_\sigma \mathbf{U} = \mathbf{E}^b, \tag{B2}$$

$$\mathbf{U} - \mathbf{P}^{\mathrm{N}}\,\mathrm{G_E}\,\Delta_\sigma \mathbf{U} = \mathbf{P}^{\mathrm{N}}\,\mathbf{E}^b. \tag{B3}$$

Note, that operators $\mathrm{G_E}\,\Delta_\sigma$, $\mathbf{P}^{\mathrm{N}}\,\mathrm{G_E}\,\Delta_\sigma$, $(\mathrm{I} - \mathrm{G_E}\,\Delta_\sigma)^{-1}$, $\left(\mathrm{I} - \mathbf{P}^{\mathrm{N}}\,\mathrm{G_E}\,\Delta_\sigma\right)^{-1}$ are bounded (see Appendices A and C for details).

Applying operator $\mathbf{P}^{\mathrm{N}}$ to eq. (B1), we obtain

$$\mathbf{P}^{\mathrm{N}}\,\mathbf{E} - \mathbf{P}^{\mathrm{N}}\,\mathrm{G_E}\,\Delta_\sigma \mathbf{E} = \mathbf{P}^{\mathrm{N}}\,\mathbf{E}^b. \tag{B4}$$

Subtracting eq. (B3) from eq. (B1) and adding eq. (B4) gives

$$\mathbf{E} - \mathbf{U} - \mathbf{P}^{\mathrm{N}}\,\mathrm{G_E}\,\Delta_\sigma(\mathbf{E} - \mathbf{U}) = \mathbf{E} - \mathbf{P}^{\mathrm{N}}\,\mathbf{E}. \tag{B5}$$

Therefore, $\mathbf{E} - \mathbf{U} = \left(\mathrm{I} - \mathbf{P}^{\mathrm{N}}\,\mathrm{G_E}\,\Delta_\sigma\right)^{-1}(\mathbf{E} - \mathbf{P}^{\mathrm{N}}\,\mathbf{E})$ and using eq. (A9), we write

$$\|\mathbf{E} - \mathbf{U}\| \le S\left\|\mathbf{E} - \mathbf{P}^{\mathrm{N}}\,\mathbf{E}\right\|. \tag{B6}$$

Subtracting eq. (B2) from eq. (B1), and using eq. (B5), we obtain

$$\tilde{\mathbf{E}} - \mathbf{E} = \mathrm{G_E}\,\Delta_\sigma \left(\mathrm{I} - \mathbf{P}^{\mathrm{N}}\,\mathrm{G_E}\,\Delta_\sigma\right)^{-1}(\mathbf{E} - \mathbf{P}^{\mathrm{N}}\,\mathbf{E}). \tag{B7}$$

Hence,

$$\left\|\tilde{\mathbf{E}} - \mathbf{E}\right\| \le C_E^{\mathrm{in}}\left\|\mathbf{E} - \mathbf{P}^{\mathrm{N}}\,\mathbf{E}\right\|, \tag{B8}$$

where

$$C_E^{\mathrm{in}} = \|\mathrm{G_E}\,\Delta_\sigma\|S. \tag{B9}$$

The estimation for $\left\|\tilde{\mathbf{H}} - \mathbf{H}\right\|$ can be obtained in a similar manner giving

$$\left\|\tilde{\mathbf{H}} - \mathbf{H}\right\| \le C_H^{\mathrm{in}}\left\|\mathbf{E} - \mathbf{P}^{\mathrm{N}}\,\mathbf{E}\right\|, \tag{B10}$$

where

$$C_H^{\mathrm{in}} = \|\mathrm{G_H}\,\Delta_\sigma\|S. \tag{B11}$$

Estimates for upper bounds for $\|\mathrm{G_E}\,\Delta_\sigma\|$ and $\|\mathrm{G_H}\,\Delta_\sigma\|$ are presented in Appendix C. Note that the errors in eqs (B8) and (B10) are estimated in $\mathcal{L}_2$ norm, due to the singularities in integral kernels in eqs (2) and (3) when $M \in \Omega$. At the same time for $M \notin \Omega$, these kernels are smooth, so we can obtain pointwise estimates.

To obtain an estimate for $\left|\tilde{\mathbf{E}}(M) - \mathbf{E}(M)\right|$ for $M \notin \Omega$, let us subtract eq. (11) from eq. (2)

$$\mathbf{E}(M) - \tilde{\mathbf{E}}(M) = \int_\Omega \widehat{G}_E(M, M_0)\Delta_\sigma(M_0)(\mathbf{E}(M_0) - \mathbf{U}(M_0))d\Omega_{M_0}. \tag{B12}$$

Then, for tensor $\widehat{G}_E(M, M_0)$, we can write

$$\widehat{G}_E(M, M_0) \le C'_E(M) = \max_{M_0 \in \Omega}\left|\widehat{G}_E(M, M_0)\right|. \tag{B13}$$

Finally, using the Schwarz inequality, we arrive at the desired estimate

$$\begin{aligned}\left|\tilde{\mathbf{E}}(M) - \mathbf{E}(M)\right| &\le C'_E(M)\max_\Omega|\Delta_\sigma|\sqrt{V_\Omega}\|\mathbf{E} - \mathbf{U}\| \\ &\le C_E^{\mathrm{out}}(M)\left\|\mathbf{E} - \mathbf{P}^{\mathrm{N}}\,\mathbf{E}\right\|,\end{aligned} \tag{B14}$$

where

$$C_E^{\mathrm{out}}(M) = C'_E(M)\max_\Omega|\Delta_\sigma|\sqrt{V_\Omega}S, \tag{B15}$$

and where V_Ω is the volume of domain Ω. The estimate for $\left|\tilde{\mathbf{H}}(M) - \mathbf{H}(M)\right|$ can be obtained similarly

$$\left|\tilde{\mathbf{H}}(M) - \mathbf{H}(M)\right| \le C_H^{\mathrm{out}}(M)\left\|\mathbf{E} - \mathbf{P}^{\mathrm{N}}\,\mathbf{E}\right\|, \tag{B16}$$

where

$$C_H^{\mathrm{out}} = C'_H(M)\max_\Omega|\Delta_\sigma|\sqrt{V_\Omega}S \quad C'_H(M) = \max_{M_0 \in \Omega}\left|\widehat{G}_H(M, M_0)\right|. \tag{B17}$$

APPENDIX C: MORE ON ESTIMATIONS OF OPERATORS' NORMS

Using eq. (A2), we first write

$$\|\mathrm{G_E}\| \le \frac{1}{\min\limits_\Omega \mathbf{Re}\,\sigma_b}. \tag{C1}$$

Then, taking into account that $\left\|\mathbf{P}^{\mathrm{N}}\right\| = 1$ by design, we have

$$\left\|\mathbf{P}^{\mathrm{N}}\,\mathrm{G_E}\,\Delta_\sigma\right\| \le \|\mathrm{G_E}\,\Delta_\sigma\| \le \frac{\max\limits_\Omega|\sigma_a - \sigma_b|}{\min\limits_\Omega \mathbf{Re}\,\sigma_b}. \tag{C2}$$

Obtaining estimates for $\|\mathrm{G_H}\|$ in terms of σ_a, σ_b and ω is much more complicated and is beyond the scope of this paper. However, the boundedness can be proved by using the following property of elliptic partial differential equations (*cf.* Gilbarg & Trudinger 2001)

$$\|U\|_{W_2^1[\Omega]} \le C(\Omega, \Omega')\left(\|U\|_{L_2[\Omega']} + \|\mathrm{L}\,U\|_{L_2[\Omega']}\right), \tag{C3}$$

where L is the elliptic partial differential operator, $\Omega \supset \Omega'$ and $C(\Omega, \Omega') > 0$ is independent of U.

Let us introduce $\mathbf{V} = \mathrm{G_E}\,\Delta_\sigma \mathbf{U}$, then V_γ is the solution of the following equation $\mathrm{L}\,V_\gamma = \Delta_\sigma U_\gamma, \gamma = \{x, y, z\}$ with corresponding elliptic operator $\mathrm{L} = \Delta + i\omega\mu_0\sigma_b$ (*cf.* Ward & Hohmann 1988). Taking into account eqs (C1) and (C3) and expressing $\mathrm{G_H}$ as $\mathrm{G_H} = \frac{1}{i\omega\mu_o}\,\mathrm{curl}\,\mathrm{G_E}$, we obtain

$$\begin{aligned}\|\mathrm{G_H}\,\Delta_\sigma \mathbf{U}\|_{L_2[\Omega]} &= \frac{1}{\omega\mu_0}\|\mathrm{curl}\,\mathbf{V}\|_{L_2[\Omega]} \le \frac{1}{\omega\mu_0}\|\mathbf{V}\|_{W_2^1[\Omega]} \\ &\le \frac{1}{\omega\mu_0}C\left(\|\mathbf{V}\|_{L_2[\Omega']} + \|\Delta_\sigma \mathbf{U}\|_{L_2[\Omega']}\right) \\ &\le \frac{C}{\omega\mu_0}\left(\|\mathrm{G_E}\| + 1\right)\max_\Omega|\sigma_a - \sigma_b|\,\|\mathbf{U}\|_{L_2[\Omega]}.\end{aligned} \tag{C4}$$

Note that we can use Ω in $\|\mathbf{U}\|_{L_2[\Omega]}$ in eq. (C4) instead of Ω' because $\Delta_\sigma = 0$ outside of Ω. Finally, assuming that $\mathbf{Re}\,\sigma_b(M) > 0$, $M \in \Omega'$ and using eqs (C1) and (C4), we obtain the desired estimate for $\|\mathrm{G_H}\,\Delta_\sigma\|$

$$\|\mathrm{G_H}\,\Delta_\sigma\| \le C(\Omega, \Omega')\frac{\max\limits_\Omega|\sigma_a - \sigma_b|}{\omega\mu_0}\left(\frac{1}{\min\limits_{\Omega'}\mathbf{Re}\,\sigma_b} + 1\right). \tag{C5}$$